This is an *Accepted Manuscript*, which has been through the Royal Society of Chemistry peer review process and has been accepted for publication.

Accepted Manuscripts are published online shortly after acceptance, before technical editing, formatting and proof reading. Using this free service, authors can make their results available to the community, in citable form, before we publish the edited article. We will replace this *Accepted Manuscript* with the edited and formatted *Advance Article* as soon as it is available.

You can find more information about *Accepted Manuscripts* in the **Information for Authors**.

Please note that technical editing may introduce minor changes to the text and/or graphics, which may alter content. The journal's standard **Terms & Conditions** and the **Ethical guidelines** still apply. In no event shall the Royal Society of Chemistry be held responsible for any errors or omissions in this *Accepted Manuscript* or any consequences arising from the use of any information it contains.

Reducing the inversion degree of MnFe$_2$O$_4$ nanoparticles through synthesis to enhance magnetization; Evaluation of their ^{1}H NMR relaxation and heating efficiency

K Vamvakidis,[a] M Katsikini,[b] D Sakellari,[b] E C Paloura,[b] O Kalogirou[b] and C Dendrinou-Samara[a],*

[a]Department of Chemistry, Aristotle University of Thessaloniki, 54124 Thessaloniki, Greece;

[b]Department of Physics, Aristotle University of Thessaloniki, 54124 Thessaloniki, Greece

*E-mail: samkat@chem.auth.gr

Abstract

Manganese ferrite ($MnFe_2O_4$) nanoparticles of identical size (9 nm) and different inversion degree have been synthesized under solvothermal conditions as a candidate theranostic system. In this facile approach, a long-chain amine, oleylamine, is utilized as reducing and surface-functionalizing agent. The synthesized nanoparticles showed cubic-spinel structure as characterized by TEM and XRD patterns. Control over their inversion degree achieved by a simple change of manganese precursor from $Mn(acac)_2$ to $Mn(acac)_3$. The variation in the inversion degree is ascribed to the partial oxidation of Mn^{2+} to Mn^{3+}, as was evidenced by X-ray absorption near edge structure and extended X-ray absorption fine structure spectroscopies at both the Fe and Mn K-edges. The reduction of the inversion degree from 0.42 to 0.22 is close to the corresponding bulk value 0.20 and led to elevated magnetization (65.7 emu/g), in contrast to Néel Temperature, which was decreased owning to weaker superexchange interactions between tetrahedral and octahedral sites within the spinel structure. In order to evaluate the performance of these nanoprobes as a possible bifunctional targeting system, the ^1H NMR relaxation of the samples has been tested together with their specific loss power under an alternating magnetic field as a function of concentration. The hydrophobic as prepared $MnFe_2O_4$ nanoparticles converted to hydrophilic with cetyltrimethylammonium bromide (CTAB). The well-dispersed in aqueous media $MnFe_2O_4$ nanoparticles showed r_2 relaxavity up to 345.5 mM^{-1} s^{-1} and heat release up to 286 W/g, demonstrated their potential use for bioapplications.

Keywords: manganese ferrite nanoparticles, solvothermal synthesis, X-ray absorption fine structure, theranostic, spinel structure

1. Introduction

Several forms of magnetism exist in nature, with superparamagnetism seeming to be preferred only in magnetic nanoparticles (MNPs), rendering them excellent candidates in numerous biomedical applications.[1,2,3] Until now, conventional nanoparticle systems have been used separately to achieve various aspects of disease management, while their greatest clinical success has been in Magnetic Resonance Imaging (MRI)-based investigations.[4] However, the push provided by advances in nanotechnology and the call for effective, specific and personalized medicine have enabled the need for combination of diagnostic and therapeutic capabilities into a single agent, called theranostic.[5] Recent developments have heightened the need for multifunctional MNPs which may be used as contrast agents in MRI and as heat nanosourses in targeted cancer therapy by means of Magnetic Hyperthermia (MH).[6,7] Many challenges remain to overcome gaps in technical knowledge and capabilities which continue to prevent progress from the bench to the bedside. One of the most crucial parameter for the effective response of a theranostic agent is the applied concentration dose. For magnetic imaging must be as low as can be otherwise the spatial resolution of MRI is decreased. Low doses require excellent magnetic properties in order to achieve the same result with the minimum MNPs concentration.

The above technologies are not fulfilled or optimized by using exclusively the currently available iron oxides NPs (e.g. Ferridex and Resovist), since due to their oxidized state posses a limited magnetization. Manganese ferrite ($MnFe_2O_4$) nanoparticles have been of great interest for their remarkable soft-magnetic properties (low coercivity and moderate saturation magnetization) accompanied by good chemically stability and biocompatibility.[8] The ferrimagnetic oxide presents a spinel-type structure (S.G. Fd3m), comprising a face-centered cubic arrangement of oxygen ions with metal cations occupying half of the octahedral (O_h) and one-eighth of the tetrahedral (T_d) interstitial sites within the anion sublattice.[9] It is convenient to introduce the degree of inversion i, a dimensionless quantity describing relative concentration of the manganese ions on O_h sites. In terms of i the spinel chemical formula can be written as: $[Mn_{1-i}Fe_i](Mn_iFe_{2-i})O_4$, with brackets and parentheses representing the T_d (A) and O_h (B) sites, respectively. In normal spinels (i = 0) all Mn ions occupy the A sites, while in inverse spinels (i = 1) are in B positions. The inversed and normal cation arrangements are merely the limits of a continuous range of possible cation distributions satisfying the spinel symmetry.

The magnetic properties of manganese ferrite are closely related to the inversion degree underling severe changes moving from the normal to inverse structure, since the $Fe_A^{3+} - Fe_B^{3+}$ superexchange interaction is much stronger than the $Mn_A^{2+} - Fe_B^{3+}$ interaction.[10] Bulk $MnFe_2O_4$ adopts an almost normal spinel structure with low degree of inversion (i = 0.20), because both Mn^{2+} and Fe^{3+} are d^5 ions and

therefore have a zero d-orbital splitting site preference energy.[11] Usually, higher inversion degrees in manganese ferrites nanoparticles have been associated with different synthetic methods.[12] In particular the most studies converge to the fact that different preparation conditions of $MnFe_2O_4$ entail partial oxidation of manganese ions which lead to higher degree of inversion, as Mn^{3+} shows a preference for octahedral sites with higher crystal field stabilization energy.[13,14] Thus, the magnetic properties of manganese ferrite are not only related to the inversion degree but also to the oxidation state of manganese ions.[15] This conclusion is plausible since Mn^{3+} possesses different cation magnetic moment (4 μ_B) than Mn^{2+} (5 μ_B). The experimentally determined magnetic moment (μ) per formula unit (f.u.) for the $MnFe_2O_4$ single crystals with different degree of inversions fit reasonably well into the formula: $\mu = (5 - 2i)\ \mu_B / $ f.u.[16,17] In this regard, a low degree of inversion is required for enhanced magnetization. Variation of the inversion degree also affects the Néel temperature, which is closely related to the overall strength of the A-B interactions.[18]

The development of new applications in the fields of nanomagnetism still requires versatile synthesis routes that allow for a fine-tuning of structural and magnetic properties according to the specifications related to a given application. A great number of synthetic procedures of nanostructured magnetic materials have been proposed in recent times such as sol−gel, mechanosynthesis, or coprecipitation. However, based on our previous results[19,20,21] and in accordance with other reports,[22] solvothermal method seems to be one of the most advantageous due to its simplicity and high reproducibility without the need of vacuum systems or protective atmospheres. The employment of economical reactants, along with the possibility of dealing with a large number of experimental parameters, makes this method promising in the nanochemistry field.

In this work, we describe the preparation of $MnFe_2O_4$ nanoparticles by means of the solvothermal method, while a study of their crystal chemistry through X-ray absorption fine structure (XAFS) spectroscopy has been attempted. A simple change of manganese precursor from $Mn(acac)_2$ to $Mn(acac)_3$ resulted in $MnFe_2O_4$ nanoparticles with lower inversion degree. The impact of both the oxidation state of manganese and the inversion degree variation on the crystal structure and on the different magnetic properties has been examined. As the average sizes of the obtained nanoparticles were almost identical the direct comparison among them was reliable. Moreover, in order to evaluate the performance of these nanoprobes as a possible bifunctional targeting system, the transverse relaxation time (T_2) was obtained by means of ^1H NMR experiments and the heating efficiency of the nanocrystals was also determined by means of specific loss power (SLP) estimations.

2. Experimental details

2.1 Materials

All the reagents were of analytical grade and were used without any further purification. The products necessary for our experiments are the following: iron (III) acetylacetonate $Fe(acac)_3$ (Fluca,$\geq$97.0%), manganese (III) acetylacetonate $Mn(acac)_3$ (Aldrich, $\geq$ 99.9%), manganese (II) acetylacetonate $Mn(acac)_2$ (Aldrich, $\geq$ 99.9%), diphenyl ether (PHE) (b.p. 259 ˚C) (Aldrich, $\geq$ 99%), oleylamine (OLM) (Aldrich, $\geq$ 70%), cetyltrimethylammonium bromide (CTAB) (Aldrich, $\geq$ 99%), chloroform (Aldrich, $\geq$ 99%) . Milli-Q water was used with a resistivity no less than 18.2 MΩ cm^{-1}.

2.2 Synthesis of manganese ferrite nanocrystals

The general synthetic procedure for the preparation of the MNPs was as follows: $Fe(acac)_3$ (1.8 mmol, 0.636 g) and $Mn(acac)_2$ (0.9 mmol, 0.228 g) were mixed and dissolved in a mixture of oleylamine (4 mL) and phenyl ether (10 mL). The resulting solution was stirred thoroughly and then transferred into a 23 mL Teflon-lined stainless-steel autoclave. The crystallization was carried out under autogenous pressure at temperature of 200 °C for 24 h. Then the autoclave was cooled naturally to room temperature and after centrifugation at 5000 rpm, the supernatant liquids were discarded and a black-brown precipitate was obtained and washed with ethanol, at least three times, to remove the excess of ligands and the unreacted precursors. In sample S2, $Mn(acac)_2$ replaced with $Mn(acac)_3$ while the rest conditions were kept constant. Samples S3 and S4 performed in the presence of pure OLM (14 mL), with the use of $Mn(acac)_2$ and $Mn(acac)_3$, respectively, as manganese source. The four different syntheses procedures are summarized in Table 1.

2.3 Preparation of water-soluble nanoparticles

In a general preparation cetyltrimethylammonium bromide (CTAB) was added to Milli-Q water to form solution A (0.1M), which was sonicated to completely dissolve the cationic surfactant. Hydrophobic nanocrystals (5 mg) were dissolved in chloroform (1–2 mL) to form solution B. Solutions A and B were mixed together with vigorous stirring and the chloroform was removed by sonication to finish the encapsulation.

2.4 Characterization

Phase identification was performed using a 2-cycle Rigaku Ultima + diffractometer (40 kV, 30 mA, CuKa radiation) with Bragg–Brentano geometry (detection limit 2% approximately). Conventional TEM images were obtained with a JEOL 100 CX microscope (TEM), operating at an acceleration voltage of 100kV. For TEM observations we have used suspensions of the nanoparticles deposited onto carbon-coated copper TEM grids. The elemental composition of the samples was tested by inductively coupled plasma atomic emission spectroscopy (ICP-AES), Perkin-Elmer Optima 3100XL and by scanning electron microscopy (SEM: JEOL 840A), where energy dispersive X-ray spectrometry (EDS) spectra were obtained. Fourier transform infrared spectroscopy (280-4000 cm^{-1}) was recorded using a Nicolet FT-IR 6700 spectrometer with samples prepared as BrK pellets. Thermogravimetric analysis (TGA) was performed using SETA-RAM SetSys-1200 and carried out in the range from room temperature to 800 ^0C at a heating rate of 10 ^0C min^{-1} under N_2 atmosphere. The X-ray absorption fine structure (XAFS) and X-ray fluorescence (XRF) measurements were conducted at the synchrotron radiation storage ring BESSY-II of the Helmholtz Zentrum Berlin at the KMC-II beamline that is equipped with a double SiGe graded crystal monochromator. The XAFS spectra were recorded at the Fe- and Mn-K-edges in the transmission mode. The near-edge X-ray absorption fine structure (XANES) spectra were subjected to linear background subtraction and normalization to the edge jump. The $\chi(k)$ spectra that result after subtraction of the atomic background and transformation from the energy- to the k-space of the extended X-ray absorption fine structure (EXAFS) spectra were fitted with the FEFFIT program with the photoelectron scattering paths constructed using the FEFF8 code.[23] The XRF spectra were recorded using the Röntec-XFlash energy dispersive detector positioned at right angle to the beam (45˚-45˚ geometry). Magnetic measurements were performed using a superconducting quantum interference device (SQUID, Quantum Design MPMS-5) and included hysteresis loops at 5 and 300K. For the zero-field-cooled/filed-cooled (ZFC/FC) measurements the samples were cooled from room temperature down to 5 K without applying a magnetic field and then heated back to room temperature under a magnetic field of 50 Oe. The Néel temperature values, were determined using vibrating sample magnetometry (VSM) (P.A.R. 155) performed over the temperature range from 300 to 800 K in fields up to 1 kOe. Hydrodynamic diameters and ζ-potentials were determined by electrophoretic measurements, carried out at 25 °C by means of a NanoZetasizer, Nano ZS Malvern apparatus (DLS). The incident light source was a 4 mW He–Ne laser at 633 nm and the intensity of the scattered light was measured at 173°. Transverse (T_2) relaxation times were measured with an Agilent NMR spectrometer (500 MHz / 9 T) equipped with VNMRJ 3.1 software at 20 °C. A CPMG pulse sequence was used to measure T_2. Hyperthermia measurements were made using a water-cooled coil, producing an alternating magnetic field (AMF) with 765 kHz frequency and

250 Oe (20 kA/m) amplitude. In all measurements, 1 ml of aqueous $MnFe_2O_4$ nanoparticles dispersion was used and subjected to the AMF. Temperature data in these experiments were taken using a fiber optic temperature probe.

Table 1 Summary of syntheses

Sample	Precursors	Solvent	Surfact.
S1	$Fe(acac)_3$, $Mn(acac)_2$	PHE	OLM
S2	$Fe(acac)_3$, $Mn(acac)_3$	PHE	OLM
S3	$Fe(acac)_3$, $Mn(acac)_2$	OLM	OLM
S4	$Fe(acac)_3$, $Mn(acac)_3$	OLM	OLM

3. Results and discussion

3.1 Structural and surface characterization

The synthesis of manganese ferrite nanoparticles coated with oleylamine was carried out using solvothermal conditions, by the decomposition of metal precursors in the presence or not of a high boiling point solvent (PHE) (Table 1). In order to evaluate the effect of the precursor valence on the inversion degree, the procedure was examined with the trivalent manganese acetylacetonate (S2 and S4). Taking advantage of the multifunctional capabilities of oleylamine[24] (solvent, reducing and capping agent) and based on our previous results[19,20,21] we performed the syntheses according to a solvent-free solvothermal process where oleylamine was used in a triple role (S3 and S4). In this case the portion of oleylamine was increased (14 mL), to preserve the same filling capacity of the autoclave (50%).

Fig. 1 presents the XRD patterns of the samples which were refined, including peak broadening due to crystallite size, using the Rietveld method. The structure refinement presents good values of the reliability factors with a goodness of fit χ^2 varying from 1.3 to 4.2 and Rp and Rwp parameters ranging from 5.49 to 8.6% and 7.07 to 11.9%, respectively. S1 and S2 showed the formation of a cubic structure (S.G. Fd3m), while the absence of any extra peak in the patterns ensures that the samples are phase pure. All the peaks are well matched with the standard JCPDS data for $MnFe_2O_4$ (file No. 10-0913). Taking the full width at half-maximum (FWHM) of the most intense peak (311) obtained from the refinement and based on the Scherrer equation the average crystalline sizes were resulted almost the same, $d_{XRD} \sim 9.0$ nm (S1: 9.1 nm, S2: 8.8 nm). The corresponding refined lattice parameters (α) of S1 and S2 were found to be 8.489(9) and 8.498(3) Å respectively, close to the bulk value (8.499 Å). Although, the two spectra reveal the same phase and crystallite size there is a qualitative difference in their intensities. The higher intensity ratio of the I_{220}/I_{400} reflection maxima in the case of S1 (1.54) compared with that corresponding to the S2

(1.26), indicates that the first presents a spinel structure closer to the inverse one than that of S2.[25] This statement is also supported by the slight difference in the lattice constants, as an inversed spinel should have smaller parameter than a normal spinel containing the same cations.[26] However, accurate estimation of the inversion degree is possible only with more powerful techniques, like X-ray absorption spectroscopy and is presented below.

For samples S3 and S4, where oleylamine was used in a triple role, contaminations of other iron and manganese oxides phases were observed (Fig. 1). In S3 three additional low-intensity peaks are present which do not belong to the spinel structure. The peaks at 24.2°, 33.2° and 41.8° can be attributed to the hematite (α-Fe_2O_3/ JCPDS, file No. 79-1741), while the two peaks at 31.3° and 45.1° reveal the presence of the tetragonal hausmannite (Mn_3O_4/ JCPDS, file No. 65-1123). The same extra phases are detected in S4, but Mn_3O_4 is present in a lower amount. The crystallite diameters of $MnFe_2O_4$ phase were approximately 7 nm for both samples while the extra phases show nanocrystals larger than > 50 nm, as estimated from the refinement.
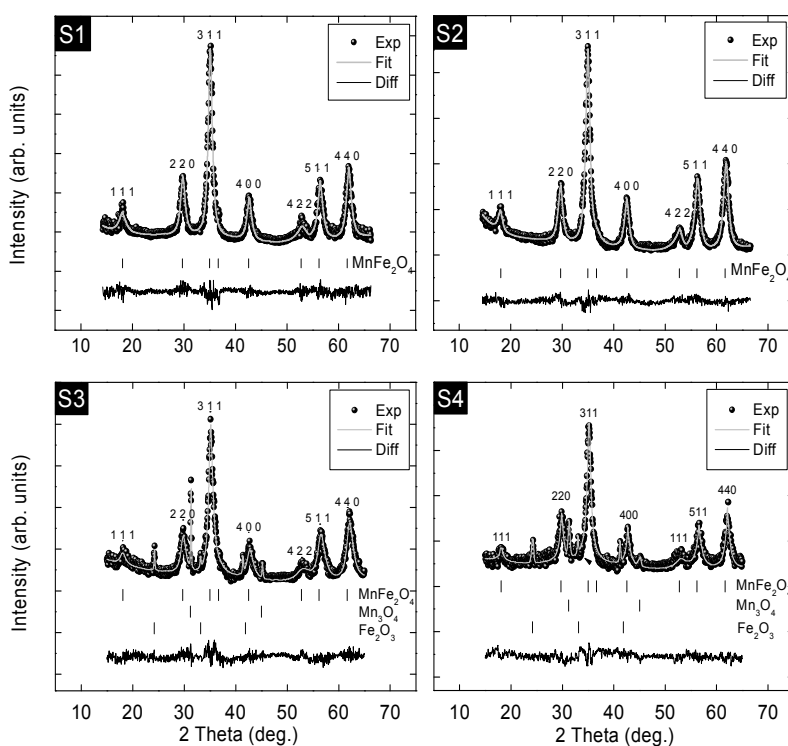

Fig. 1 Measured diffraction patterns of samples S1, S2, S3, S4 and Rietveld refinements.

TEM imaging was employed to investigate further the morphologies and crystallographic features of the single phases. The bright-field image (Fig. 2a) of sample S1 clearly shows nearly spherical nanoparticles with broad size distribution, while for sample S2 (Fig. 2c) the same phase and shape are observed although the size distribution is reduced. Representative selected area electron diffraction

8

(SAED) patterns can be indexed as the cubic spinel structure of $MnFe_2O_4$ phase and supports the single crystalline nature of the samples (Fig. 2b and 2d). The histograms of particle size distributions (insets in Fig. 1a, 1c) were built by counting 200 particles for each sample and were fitted with a standard normal function. The average nanoparticle sizes d_{TEM} were found 8.6 ± 0.9 and 8.2 ± 0.5 nm, for S1 and S2 respectively, close to the corresponding ones from the XRD patterns. In Fig. 2Sa and 2Sb (†ESI) are displayed a representative EDS spectrum taken from sample S1 and a XRF spectrum taken from sample S2. Both techniques show the presence of Fe and Mn in an atomic ratio 2/1. For the XRF measurements the elemental sensitivities were taken into account. The chemical composition analysis was also measured by ICP-AES and has revealed the same stoichiometry in both samples.
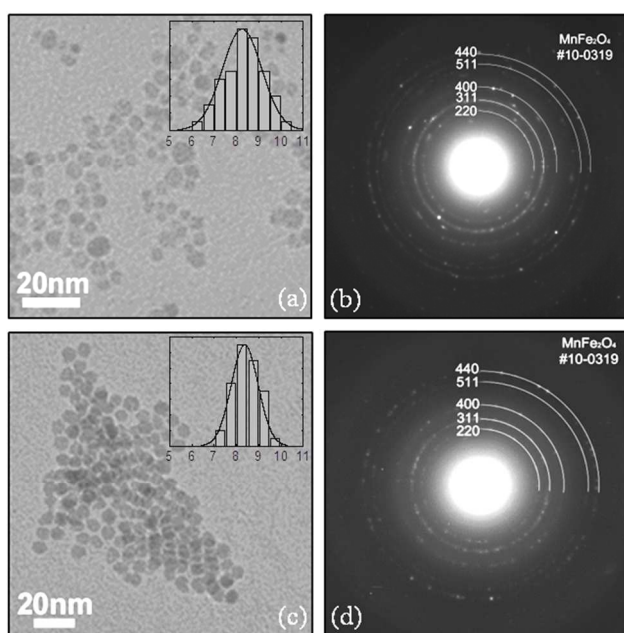

Fig. 2 TEM images and particle size distribution histograms (insets) of: S1(a) and S2 (c). Diffraction patterns of: S1 (b) and S2 (d), which can be indexed to crystalline planes of the $MnFe_2O_4$ structure.

FT-IR spectroscopy was applied for the characterization of the surface of the $MnFe_2O_4$ nanoparticles (†ESI Fig. 1Sa). The corresponding spectra of the samples S1 and S2 revealed absorption bands in a good agreement with OLM molecule shown also as reference. The high frequency bands observed in the region 2926 and 2853 cm^{-1} are characteristic for the asymmetric (v_{as}) and symmetric (v_s) stretching vibrations of methylene groups (–CH$_2$). At 1640 cm^{-1} the low intensity peak is assigned to the stretching vibration of the double bond δ(-C=C), and the peak at 1588 cm^{-1} is attributed to NH$_2$ group, found shifted to some extent due to interactions with the metal core. Finally, the peak at 1438 cm^{-1} is attributed to C-H bending in methylene groups,[27] while the typical low frequency band at around 575 cm^{-1}

refers to motion of oxygen with respect to the cations in the T_d and O_h sites, characteristic of the spinel structure.[28] The amount of surfactants coated on the surface was quantitatively recorded by thermogravimetric analysis (TGA), (†ESI Fig. 1Sb). The decomposition of the organic coating occurs in a similar way for both samples. The content of oleylamine was estimated 20% and 23% for S1 and S2 respectively, by measuring the mass reduction in the range of 100-800 ˚C. The early weight loss until 100 ˚C can be ascribed to the removal of physically adsorbed water molecules. Two steps of mass reduction were observed after 100 ˚C stemmed from the hydrocarbon chains and the nitrogen head groups. The chain decomposition occurs at 200~450 ˚C, while the removal of the amine group takes place at higher temperatures indicating the bonding with the metal core.[29]

3.2 XAFS spectroscopy

The bonding environment of Mn and Fe was studied by means of XAFS spectroscopy. Fig. 3 shows the XANES spectra of samples S1 and S2 recorded at the Mn and Fe-K-edges. The characteristic pre-edge peak has been assigned to 1s➔3d transitions which become dipole allowed after mixing of the metal d with 4p states.[30] The formation of non-centrosymmetric polyhedra around the absorbing metal atom, as for example tetrahedral, results in enhancement of the pre-edge peak intensity. The position of the pre-edge peak is affected by the oxidation state of the metal. In the case of the Fe-K-edge XANES spectra the position of the pre-edge peak is characteristic of Fe^{3+} in octahedral coordination. The small red shift of the pre-edge peak in the spectrum of the S1 sample is an indication of a slight increase of tetrahedral contribution.[8] The centroid position of the pre-edge peak in the Mn-K-edge spectra is found in between the corresponding positions for Mn^{2+} and Mn^{3+} taking into account reference compounds.[31] The slight red-shift of the pre-edge peak of the S2 sample relative to S1 is attributed to lower value of the oxidation state of Mn. The smaller percentage of Mn atoms having 3+ oxidation state in the sample S2 is also verified by the 0.25 eV red-shift of the position of the absorption edge relative to the corresponding position of the sample S1.[32] Therefore, the number of Mn^{3+} ions in S2 is smaller and a lower inversion degree is expected.
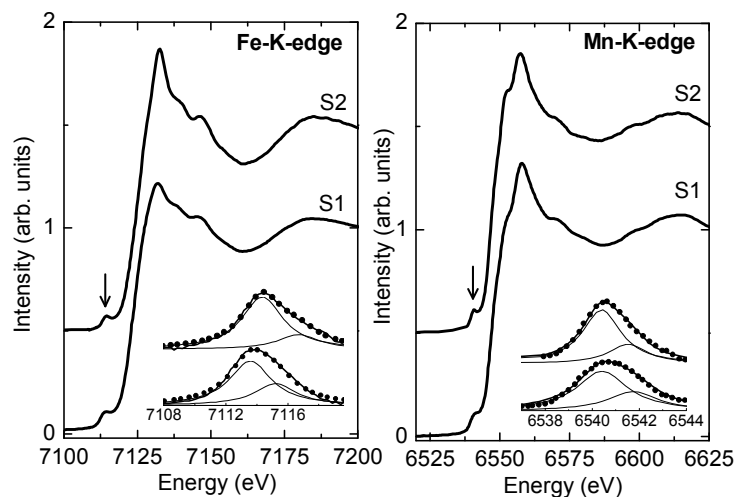
Fig. 3 Normalized XANES spectra recorded at the Fe- and Mn K-edge of the S1 and S2 samples. The total area under the pre-edge peaks (indicated by an arrow) was estimated by fitting with two Lorentzian functions, as shown in the insets.

In order to obtain quantitative information on the degree of inversion, the EXAFS spectra were fitted up to the distance of 4 Å using proper models of spinel ferrites and taking into account that the absorbing Fe of Mn atoms may occupy tetrahedral sites (hereafter called Fe_A and Mn_A) and octahedral sites (denoted as Fe_B and Mn_B). Given that the atomic number of Fe and Mn differs only by 1 the two atoms have similar backscattering amplitudes. Therefore in order to reduce the uncertainty, only Fe backscatterers were considered in the fitting. The distribution of Mn and Fe cations between tetrahedral and octahedral sites was taken into account using the variable parameters, $x_B(Mn)$ and $x_B(Fe)$ that indicate the fraction of Mn and Fe cations, respectively occupying octahedral sites. The rest of the atoms occupy tetrahedral sites i.e. $x_A(Mn)=1-x_B(Mn)$ and $x_A(Fe)=1-x_B(Fe)$. Under this description, the parameter $x_B(Mn)$ corresponds to the inversion parameter, i. Photoelectron scattering paths of the tetrahedral and octahedral contributions that were characterized by similar nearest neighbor distances, were merged together using proper coordination numbers in order to reduce the uncertainty of the fitting. Otherwise a separate scattering path was considered. During the fitting the coordination numbers were kept fixed to the values predicted by the symmetry, whereas the $x_B(Mn)$ and $x_B(Fe)$ values were allowed to vary. The nearest neighbor distances at distant shells (R > 3 Å) were kept fixed according to the values determined by XRD. A multiple scattering (triangular) path at the distance of approximately 3.8 Å was also used. Each one of the contributions in the triangular path was set equal to the length of the corresponding single scattering paths. The $\chi(k)$ spectra and the corresponding Fourier transforms of the spectra for the samples S1 and S2 recorded at the Fe- and Mn-K-edges are shown in Fig. 4. The fitting results are listed in Table 2.
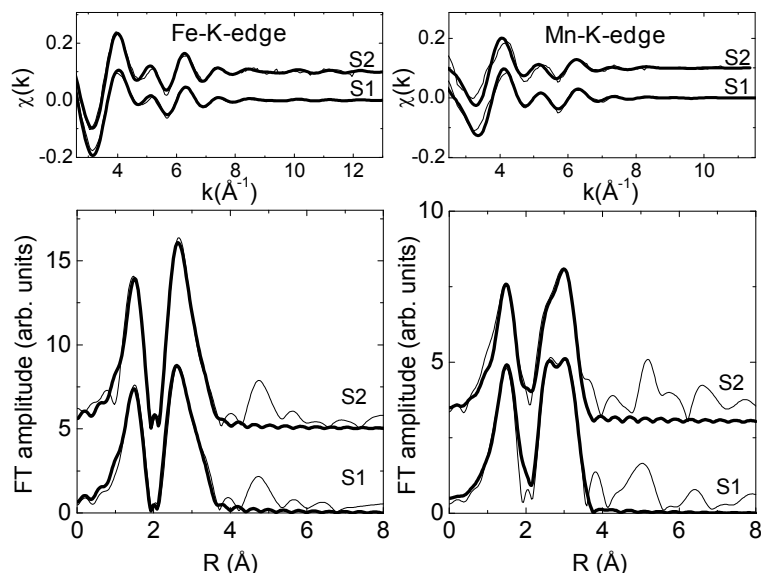
Fig. 4 Fe- and Mn-K-edge $\chi(k)$ spectra and Fourier transforms of the k^3-weighted $\chi(k)$ spectra. The experimental and fitting curves are shown in thin and thick solid lines, respectively.

According to the results listed in Table 2, the first nearest neighbor distances differ depending on the type of polyhedra formed by the metal (the notation A and B stands for tetrahedra and octahedra, respectively) and also on the type of the central atom. More specifically, the $Fe_A(Mn_A)$–O distance is approximately 0.15 Å shorter than the $Fe_B(Mn_B)$–O distance and all the Fe–O distances are shorter by approximately 0.15 Å compared to the Mn–O distances. At further shells the distances predicted by XRD seem to fit properly the spectra. It should be noted that the characteristic splitting observed in the 3–4 Å distance range of the Fourier transform of the Mn-K-edge spectra with enhanced low-R intensity is attributed to the higher occupation of octahedral sites. It should be noted that at the distance of approximately 3 Å only the octahedral coordination has significant contribution. In sample S2 this peak is reduced significantly compared to sample S1, displaying the small number of manganese ions in the octahedral sites. The results of the fitting confirm that the degree of inversion decreases from 0.42 (S1) to 0.22 (S2). The stoichiometry of the spinel ferrites requires that: $x_B(Fe) = 1- x_B(Mn)/2$.[8] The slight deviation from this equation for the sample S1 could be attributed to the presence of vacancies. According to the XANES characterization, this sample is expected to contain more Mn^{3+}. The partial oxidation of Mn^{2+} to Mn^{3+} results in the formation of vacancies in the octahedral sites for charge neutrality reasons, taking into account that the samples are stoichiometric and that Mn^{3+} occupies octahedral sites.[8,33]

Table 2 Fitting results of the Fe- and Mn-K-edge EXAFS spectra. R are the nearest neighbor distances, N the coordination numbers, σ^2 the Debye–Waller factors and $x_B(Mn)$, $x_B(Fe)$ the fraction of Mn and Fe atoms that occupy octahedral sites. Values of r-factor that correspond to the simultaneous fitting of the spectra recorded at the two edges are also reported. MS refers to a triangular multiple scattering path

Shell	Fe-K-edge			Mn-K-edge		
	N	R (Å)	σ^2 (Å^2)	N	R (Å)	σ^2 (Å^2)
Sample: S1 (r-factor = 0.06076)						
[$x_B(Mn) = 0.42 \pm 0.03$, $x_B(Fe) = 0.87 \pm 0.03$]						
O (O_h)	5.2	1.97	0.0101	2.5	2.09	0.0087
O (T_d)	0.5	1.81	0.0091	2.3	1.94	0.0073
Fe (O_h)	5.1	3.00	0.0096	2.4	2.98	0.0116
Fe(O_h,T_d)	6.6	3.50	0.0096	9.2	3.53	0.0163
O (O_h,T_d)	3.2	3.54	0.0090	7.5	3.54	0.0119
O (T_d)	0.5	3.67	0.0110	2.2	3.67	0.0130
Fe (O_h)	5.0	3.71	0.0150	2.4	3.71	0.0189
MS	13.1	3.65	0.0173	18.3	3.68	0.0204
Sample: S2 (r-factor = 0.06409)						
[$x_B(Mn) = 0.22 \pm 0.03$, $x_B(Fe) = 0.93 \pm 0.03$]						
O (O_h)	5.6	1.98	0.0090	1.3	2.14	0.0099
O (T_d)	0.3	1.85	0.0081	3.1	1.98	0.0092
Fe (O_h)	5.5	3.01	0.0077	1.3	2.96	0.0108
Fe(O_h,T_d)	6.2	3.50	0.0084	10.4	3.52	0.0167
O (O_h,T_d)	2.6	3.53	0.0140	9.5	3.53	0.0202
O (T_d)	0.3	3.67	0.0150	3.0	3.66	0.0176
Fe (O_h)	5.4	3.71	0.0160	1.3	3.71	0.0193
MS	12.5	3.68	0.0153	20.1	3.76	0.0217

3.3 Formation aspects

In order to produce ternary metal oxides such as ferrite nanocrystals, usually two types of precursors are required for serving as different metal sources, while their decomposition temperatures must be as close as possible to obtain stoichiometrically precise materials. In particular, for Fe(acac)$_3$ and Mn(acac)$_2$ a clear difference (> 60 ˚C) of their decomposition temperatures has been reported.[34] Among the acetylacetonato complexes, the trivalent Mn, Co and Fe were found to be quite unstable and their dissociation occurs at lower temperatures, in regard to the divalent metal chelates.[35] In our experiments, the divalent precursor Mn(acac)$_2$, which is commonly used, led to MnFe$_2$O$_4$ particles of a higher level of octahedrally deposited Mn^{3+} and therefore higher inversion degree, indicating the partially oxidation of Mn^{2+} to Mn^{3+}. Oxidation process is favourable even in aprotic and degassed systems or in the presence of nitrogen atmosphere and has been several times reported.[36-38] In case of S2, the faster decomposition of

Mn(acac)$_3$ led to MnFe$_2$O$_4$ nanoparticles of a low inversion degree indicating that the reduction of Mn^{3+} to Mn^{2+}, in addition with the extra Hacac molecules which produce a stronger reductive environment, is faster than the reverse process. Meanwhile, the faster decomposition of Mn(acac)$_3$ ensures that the incorporation of manganese ions in the spinel lattice occurs simultaneously with the iron ions. Moreover, although we do not know the inversion degree of the resulted manganese ferrite of S3 and S4 the presence of different percentage of the hausmannite phase enlarged that the reduction is fast and dominant. The resulted Mn^{2+} consumed to the formation of MnFe$_2$O$_4$ and in so the percentage of hausmannite minimised (S4). Finally, the formation of hematite may be attributed to the presence of pure OLM and in connection with the mild reducing ability of the amine.[24] α-Fe$_2$O$_3$ resulted almost to the same amount in case of S3 and S4, in accordance with the respective intensities of XRD analysis. As the formation of the spinel ferrites commences with a solvolysis of the acetylacetonate species followed by ketimine condensation reactions[39] the increased amount of the amine enhanced the formation of Fe-O-Fe bonds. It is worth to mention that formation of hematite is a side reaction of dehydration of β-FeOOH into α-Fe$_2$O$_3$ and depends on the synthetic conditions and as such is given in the literature.[40]

3.4 Magnetic studies

Magnetic properties were studied by measuring the magnetization as a function of temperature and field. ZFC/FC measurements of S1 and S2, recorded from 5 to 300 K by applying a 50 Oe probe field, are shown in Fig. 5. Both samples are superparamagnetic at room temperature, as indicated by the full convergence of the ZFC/FC curves at high temperatures T>T$_{max}$. In contrast, at low temperatures (T<T$_{max}$) the curves are irreversible, showing that in this region the nanoparticles are in a blocked state, due to energy barriers of magnetic anisotropy.[41] This statement is also confirmed by the loops at 5 K (Fig. 5 insets), which reveal a hysteretic behaviour with coercive field (H$_C$), 276 and 171 Oe, respectively. The fact that FC curves do not reach a plateau as soon as T$_B$ is reached indicates that the dipolar interactions are not prevailing in both samples. It should be also noted that in the case of S1 the peak of ZFC is broader, related to the wider size distribution as supported by the TEM images (Fig. 2a). Blocking temperature (T$_B$) is not identical to T$_{max}$, as it is slightly lower. Correct estimation of T$_B$ is given by the relation: T$_B$ = T$_{max}$/1.06.[42] The obtained values were found to be 118 K (S1) and 101 K (S2). Assuming a spherical shape for the nanocrystals and that their easy magnetization axes are randomly oriented, a first rough determination of anisotropy constant is possible. The blocking temperature reflects the range for which the time scale of magnetization measurements equals the relaxation time, and thus the anisotropy constant can be estimated from the T$_B$ value of the ZFC curve:[43]

$$K_{eff} V = k_B T_B \ln(\tau / \tau_0) \qquad (1)$$

where K_{eff} is the effective anisotropy energy, V is the volume of the particle, k_B is Boltzmann's constant, τ_0 is usually called the "attempt time" and is assumed to be of the order of 10^{-9} s[44] and τ is the superparamagnetic relaxation time. However, the observation of superparamagnetic behavior depends strongly on the experimental time window (τ_{exp}). The relative values of τ and τ_{exp} will determine whether or not a non-zero magnetization is measured. A net zero magnetization will be measured if $\tau \ll \tau_{exp}$, and a non-zero magnetization will be observed if $\tau \gg \tau_{exp}$. For magnetization measurements, τ_{exp} is of the order of 100 s[45]. Using these values the following approximation is derived from equation (1): $K_{eff}V \approx 25\ k_B\ T_B$ (taking $\ln\tau/\tau_0 \approx 25$). The resulted values of K_{eff} (Table 3) are higher than those reported for manganese bulk ferrites (0.025 x 10^5 J/m³),[13] as expected for nanosized particles. In S1 there is a slight increase in anisotropy, attributed to higher magnetocrystalline anisotropy as a result of Jahn-Teller distortion of the octahedral Mn^{3+} ions.[46]
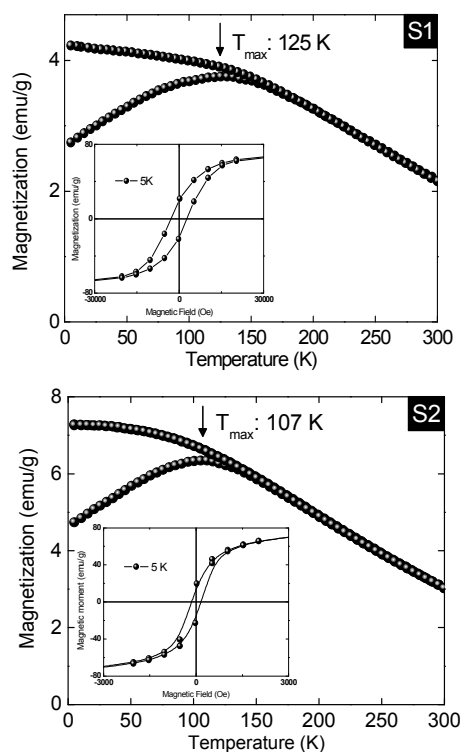

Fig. 5 ZFC/FC curves of samples S1, S2 and hysteresis loops recorded at 5 K (insets).

Hysteresis cycles at 300 K (Fig. 6) exhibit a typical superparamagnetic state with negligible coercivity and rapid saturation. The absolute values of magnetization (M_S) were estimated from the effective mass of the nanoparticles (†ESI Fig. 1Sb). The M_s of the samples were found equal to 54.6 and 65.7 emu/g for S1 and S2, respectively. These values are comparable and relatively higher, to those reported for $MnFe_2O_4$ nanoparticles with respected particle sizes.[47] The decrease of magnetization

considering the bulk value (80 emu/g), is related to the larger percentage of atoms located on the surface of the NPs, producing a magnetically dead layer. Interestingly, for the sample S2 the decline in magnetization is smaller. As the two samples posses the same size and have been stabilized by the same surfactant we believe that surface effects in both samples contribute equivalently to the decrease of magnetization. In addition the FT-IR spectra (†ESI Fig. 1Sa) reveal identical patterns, supporting isotropic binding of oleylamine molecules on surface. Therefore we can safely correlate their different magnetic performance mainly with the intrinsic properties of their magnetic core. The only unequal structural feature of these nanoparticles is their inversion degree.
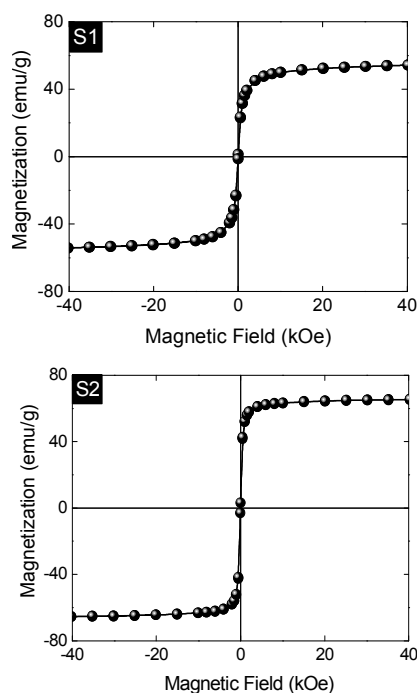

**Fig. 6** Hysteresis cycles of samples S1 and S2 recorded at 300 K.

Theoretically, in bulk manganese ferrite crystals if all the Mn ions are divalent (Mn^{2+}) and all the Fe ions are trivalent (Fe^{3+}), then the magnetic moment at 0 K is expected to be 5 μ_B / f.u., according to the Néel model[48]. However, considering that both Mn^{+2} and Fe^{+3} are d^5 ions with spin 5/2 and zero orbital momentum, this value of 5 μ_B would be independent of the inversion degree, as the distribution of metals with the same Bohr magnetons has no influence on the net magnetization. However, from magnetic scattering measurements,[49] the magnetic moment of $MnFe_2O_4$ was found to be ~4.6 μ_B / f.u. This reduced magnetic moment of $MnFe_2O_4$ has drawn much attention and different models have been proposed to explain it. According to *Harrison et al*[50] the presence of Mn^{3+} ions is prescribed which are counterbalanced by either Fe^{2+} ions or some vacancies in the spinel structure.[8] On the other hand, based

16

on Mössbauer measurements the canted spin model was proposed,[51] but nuclear magnetic resonance (NMR) experiments showed no evidence of spin canting.[49] In our case, XAFS analysis indicates clearly the existence of Mn^{3+} ions (4 μ_B) at B sites in both samples, and the absence of Fe^{2+} which denotes cation vacancies at the octahedral sites so that charge neutrality is preserved.

In spinel ferrites it is possible to calculate the net magnetic moment per formula unit at 0 K, based on Néel's two-sublattice model of ferrimagnetism:[48]

$$\mu = M_B - M_A \tag{2}$$

where M_B and M_A are the sublattice magnetic moments of B and A sites. In our case according to the model proposed by Harrison *et al.*[50] and when Fe^{2+} ions are not present in O_h sites, the chemical formula for manganese ferrite may be written as:

$$[Mn^{2+}_{1-i}Fe^{3+}_i]^A(Mn^{3+}_iFe^{3+}_{2-i})^BO_4$$
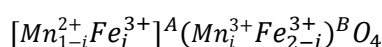
Since magnetic moments of Fe^{3+}, Mn^{2+} and Mn^{3+} are 5, 5 and 4 μ_B, respectively, the net magnetic moment (μ) per formula unit can be expressed as:

$$\mu = 5(2 - 2i) + 4i - 5i - 5(1 - i) = (5 - i)\ \mu_B\ /\ \text{f.u.} \tag{3}$$

Even though the above equation differs from the one that has been reported previously: $\mu = (5 - 2i)\ \mu_B\ /\ \text{f.u.}$[16,17] there is still the same linear dependence from the inversion degree. The difference in the two calculations arises from the fact that in our samples the presence of Fe^{2+} ions was excluded from the XAFS results. Thus, the number of μ_B per formula unit is accordingly changed. In any case, it is obvious that to enhance magnetization in $MnFe_2O_4$ nanoparticles the formation of trivalent manganese ions should be as low as possible. Mn^{3+} shows a preference for octahedral sites raising the inversion degree thus resulting to a decrease of μ as it is derived from equation 3. Compared to S1 in S2 the amount of Mn^{3+} was smaller and thus magnetization was increased.

The different distribution of the metal ions in the spinel lattice should also affect the Néel temperature (T_N). Based on the fact that in ferrimagnetic compounds both exchange integrals, J_{AA} and J_{BB}, can be considered negligible when compared to the exchange integrals J_{AB} among ions in A and B sites, a partial transfer of a number of Fe^{3+} cations from B to A sites can causes an increase of T_N.[10] Therefore, the average strength of J_{AB} is a function of the number of bonds between two Fe^{3+} ions, $Fe^{3+}_A - O^{2-} - Fe^{3+}_B$, and is raised as the inversion degree increases. T_N values for both samples (Fig. 7a) were measured and found higher (S1: 688 K and S2: 633 K) compared to that of the bulk ceramic standard (T_N = 573 K), in accordance with previously reported values of nanoscale ferrites.[18, 14, 52] However, the increase in S2 is stronger, revealing the crucial impact of inversion degree on magnetic order at different temperatures.
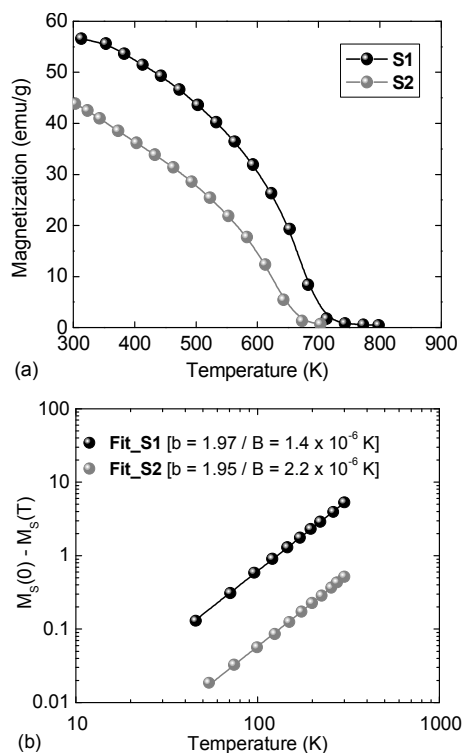
17

Fig. 7 (a) Thermomagnetic curves of S1 and S2 under the application of a 1 kOe magnetic field. (b) Depression of the core magnetization $M_S(0)-M_S(T)$ of S1 and S2 in a double logarithmic representation. The full line corresponds to the best fit using equation 5 and yields the value of b.

In order to support the influence of the inversion degree on the superexchange interactions, the J_{AB} exchange constant of both samples has been studied in more detail by fitting the FC curve to the Bloch law. The first-order term of Bloch's law describes the temperature dependence of the saturation magnetization at low temperatures due to low energy collective excitations, well known as spin waves or magnons and can be written as:

$$M_S(T) = M(0)(1 - BT^{3/2})\qquad(4)$$

where Ms(T) is the temperature-dependent saturation magnetization, M(0) is the magnetization of the ground state at 0 K and B is Bloch's constant. The value of B depends on the exchange integral J_{AB} in the following way:[53]

$$B = \frac{0.0587}{SQ}\left(\frac{k_B}{2JS}\right)^{3/2}\qquad(5)$$

where k_B is the Boltzmann constant, Q is 1, 2, and 4 for single cubic, bcc, and fcc systems, respectively and S is the total electron spin. However, for MNPs and small clusters, some theoretical calculations as well as experimental results have indicated that the temperature Bloch exponent is expected to be higher

18

than $3/2$.[14,54] The Bloch exponent (b) is for nanoscale materials size dependent and structure independent, whereas the Bloch constant (B) mainly depends on the structure features of the core of the nanoparticles, such as the superexchange interactions. The depression of the core magnetization $M_S(0)-M_S(T)$ is plotted of both samples in Fig. 7b as a function of temperature. In that log-log representation, the variations are linear with a slope representing the exponent b. In Fig. 7b are also presented the parameters B and b, obtained from the linear fitting to the Bloch's law of both samples. Almost same values for the b exponent were raised, due to the same size of NPs, but different Bloch constants, due to the different interactions.[55] Table 3 shows the corresponding values of the exchange constant J_{AB} obtained from the corresponding values of B. The calculated values are overestimated compared to the bulk,[17] since for the calculation we assumed that J_{AB} is the only interaction within lattice, which is inaccurate if a detail description is required, while surface effects was not taken into account. Moreover, in equation 5, we imported the value $5/2$ for S, assuming the same spin for both metals in each valance state, as a rough approximation. Therefore, the results can only be used only as qualitative proof that J_{AB} increases with increasing i.

Table 3 Chemical formulas according to the inversion degree of each sample and the main magnetic characteristics of the particles.

Sample	M_S (emu/g)	K_{eff} (10^5 J/m^3)	T_B (K)	T_N (K)	J_{AB} (K)
S1: $[Mn_{0.58}Fe_{0.42}](Mn_{0.42}Fe_{1.58})O_4$	54.6	0.043	118	688	-52
S2: $[Mn_{0.78}Fe_{0.22}](Mn_{0.22}Fe_{1.78})O_4$	65.7	0.039	101	633	-38

3.5 ^1H NMR relaxation

NMR studies were performed in order to evaluate farther application of the nanoparticles as contrast agents. NMR detects water protons as they relax back to their equilibrium state after a radiofrequency pulse perturbs their alignment along a strong external magnetic field. This relaxation is the combined result of two different mechanisms.[56] Longitudinal relaxation (T_1) or spin–lattice relaxation, due to energy exchange between the spins and their surroundings, and transverse relaxation (T_2), or spin–spin relaxation, due to interactions of spins between them, resulting in loss of phase coherence. Superparamagnetic nanoparticles have a much smaller effect on the T_1 water proton relaxation time than on the T_2 relaxation. In this process, the major relaxation mechanism is the dipolar outer-sphere interaction between the water proton spins and the magnetic moment of the nanoparticles. Therefore, as shown in the model suggested by Koenig and Keller, spin–spin relaxation is strongly dependent on the magnetic moment of the nanoparticles (μ):[57]

$$R_2 = \frac{1}{T_2} = \frac{\alpha}{dD}\gamma^2\mu^2 C_{NPs} J(\omega, \tau_D) \tag{6}$$

where α is a constant, d the diameter of the nanoparticle, D the diffusion coefficient, μ the magnetic moment,γ the gyromagnetic ratio of the water proton, C_{NPs} the concentration of the nanoparticles, and $J(\omega,\tau)$ the spectral density function. T_2 data were used to calculate the transverse relaxivity (r_2) (the transverse relaxation rate per mM of metal ions). The relaxation rate $(R=1/T_2)$ increases linear with the nanoparticles' concentration according to the equation:

$$\frac{1}{T_2} = \frac{1}{T_0} + r_2 C \tag{7}$$

where $1/T_2$ is the observed relaxation rate in the presence of the nanoparticles, $1/T_0$ the relaxation rate of pure water and C the concentration of MNPs.

The hydrophobic MNPs (S1 and S2) were converted to hydrophilic with the addition of CTAB molecules. This bilayer assembly is energetically favored as it ensures hydrophobic interactions between the surfactant tails and hydrophilic interactions of the positive charged head group $(-N^+(CH_3)_3)$ with the aqueous media at the nanoparticle–solvent interface. The ζ-potential of these hydrophilic MNPs was determined as an indicator of the colloidal stability of the aqueous suspensions at neutral pH. The hydrodynamic diameters were 243 nm and 180 nm (†ESI Fig. 3Sb) while ζ values found + 42.5 mV and + 36.5 mV for S1 and S2, respectively (†ESI Fig. 3Sa).

The transverse relaxation rates (R_2) were determined by means of the Carr-Purcell-Meiboom-Gill pulse sequence (CPMG). All these measurements showed perfect monoexponential decay, which is characteristic for magnetic compounds that enhance the water proton relaxivity by diffusion. As shown in Fig. 8, sample S2@CTAB exhibits the highest r_2 relaxivity, reaching 345.5 mM^{-1} s^{-1}, compared to S1@CTAB (196.6 mM^{-1} s^{-1}). Generally, r_2 increases with respect to magnetization while the effect of aggregation in the suspension has also important impact on the relaxometric properties especially when particle sizes are bigger than 9 nm.[58] The formation of aggregates can be concerned for both samples due to the increased hydrodynamic sizes. However, the difference is not substantial, taking into account that the polydispersity degree for both samples is about 0.40. Therefore, enhanced relaxivity of S2@CTAB stems mainly from the higher magnetization value. The obtained molar relaxivity of S2@CTAB is much higher compared to γ-Fe$_2$O$_3$@SiO$_2$ MNPs studied in a similar NMR spectrometer (500 MHz), as the highest r_2 value found equal to 228 mM^{-1} s^{-1} (10.0 nm γ-Fe$_2$O$_3$ NPs) with respect to the decreasing thickness of silica layer.[59] For slightly smaller manganese ferrite nanoparticles (7.6 ± 1.4 nm), following a ligand exchange procedure, where oleic acid and oleylamine were exchanged with DMSA, r_2 found 227.6 mM^{-1} s^{-1} (T_2 values recorded at 9.4 T).[60] Meanwhile, CTAB has been used previously as surfactant

in the synthesis of gold-coated manganese-ferrite nanoparticles where 12 nm core-shell NPs showed relaxivity 83.3 mM^{-1} s^{-1} (1.5 T), higher than those of commercial iron-oxide contrast agents.[61]
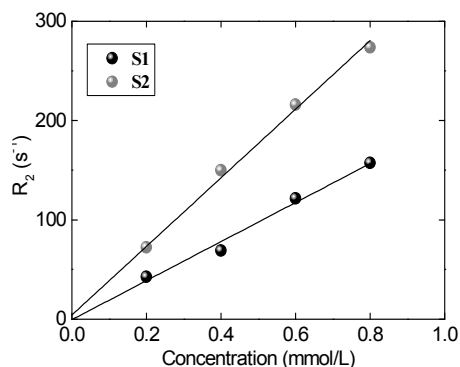

Fig. 8 R$_2$ relaxation plots of aqueous suspensions of S1@CTAB and S2@CTAB as a function of concentration.

3.6 Hyperthermia efficiency

Heat dissipation of ferrofluid produced by the delay in the relaxation of the magnetic moment is observed when superparamagnetic NPs are exposed to an alternating magnetic field of proper frequency. The heating capacity of a magnetic material is quantified by the specific loss power (SLP), defined as the amount of energy converted into heat per time and mass.[62] The SLP is calculated using the following relation:

$$SLP = C_P \frac{m_f}{m_{NPs}} \frac{\Delta T}{\Delta t} \qquad (8)$$

where C_p is the specific heat of the solution, m_f is the sample volume, m_{NPs} is the mass of magnetic material in the sample and $\Delta T/\Delta t$ the initial slope of the heating curve. Two different mechanisms compete to determine the relaxation of the magnetization:[63] the Néel relaxation, corresponding to the magnetic moment reversal over the energy barrier, characterized by $\tau_N = \tau_0 \exp(KV/k_BT)$, and the Brown relaxation, corresponding to the mechanical rotation of the whole particle, described by $\tau_B = 3\eta V_H/k_BT$ (η is the viscosity of the media and V_H is the hydrodynamic volume).

Fig. 9 shows the experimental hyperthermia curves for the hydrophilic S1@CTAB, S2@CTAB and the SLP values estimated as a function of concentration. In all cases the reference signal from the Milli-Q water was subtracted to isolate the signal resulting from the nanoparticles themselves. SLP values, recorded at 250 Oe, of S1@CTAB were found 133, 167, and 227 W/g, respectively, while for S2@CTAB consistently higher SLP values were obtained 236, 249 and 286 W/g. Taking into account that MNPs should be applied in the lowest/effective doses, 0.1 to 1 mg/mL of MNPs were used where

SLP values found to be increased respectively. S2@CTAB found to be effective even in the lowest concentration (0.1 mg/mL), as temperature rose above 42 °C in about 10 min, corresponding to the desirable hyperthermia levels (i.e 5 ˚C < ΔT < 14 ˚C, starting from basal body temperature, 37 °C). It has been proposed that as the concentration of the particles is increased and the separation among them decreases, dipolar interactions are favored.[64] These interactions can be either ferromagnetic or antiferromagnetic leading to either increase or decrease in the heating capacity. Therefore, influence of dipole interactions on magnetic heating is still under investigation. The observed increase of SLP values with concentration could be attributed to the presence of ferromagnetic interactions. Similar behavior to the studied systems has been previously observed e.g. for Fe_3O_4 nanoparticles.[65] However, an opposite result found before by us[20] and others[66] where SLP decreased with increasing concentration. Lower SLP values (148.4 W/g) have been reported recently by Doaga et al[67] for bigger nanoparticles (18.2 nm) under different experimental conditions (1.95 MHz, 29 Oe). Additionally, at 266 kHz and 653 Oe the SLP value of $MnFe_2O_4$ nanoparticles (12.1 nm) was 1.45 W/g, as reported by Kim et al[68], while at 231 kHz and 653 Oe the heating efficiency of smaller nanoparticles (10.5 nm) was better (500 W/g).[69] Hence, experimental conditions, optimal chain size of surface coating and particle diameter all contribute significantly to heating, and certain assessment is very difficult; further magnetization measurements (ferromagnetic resonance) are needed and/or Monte Carlo simulations to provide insights into the pronounced dependence of SLP.[70]
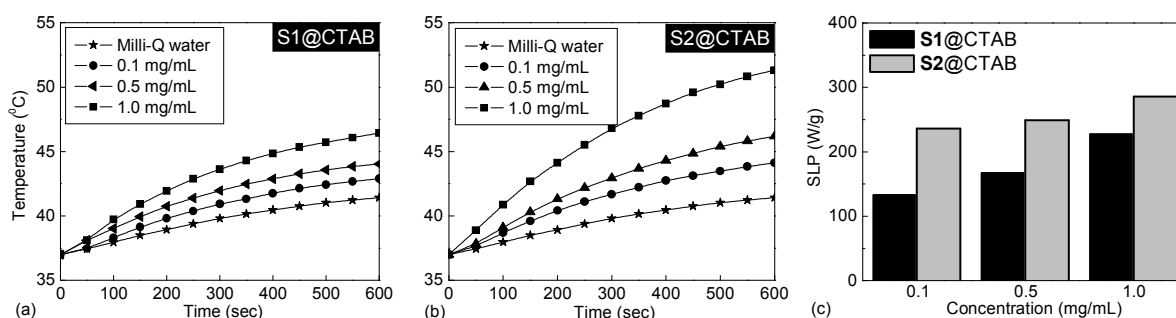

Fig. 9 Temperature versus time curves of (a) S1@CTAB and (b) S2@CTAB. (c) Concentration dependence of SLP values of the samples.

4. Conclusions

Monodispersed $MnFe_2O_4$ MNPs of identical size (9.0 nm) and different inversion degree have been solvothermally synthesized in diphenyl ether and in the presence of OLM. The alternate application of $Mn(acac)_3$ as precursor instead of $Mn(acac)_2$, allowed us to reduce the inversion degree from 0.42 to 0.22, as supported by XAFS analysis, due to the partial oxidation of Mn^{2+} to Mn^{3+}, which results in octahedral

coordinated manganese ions within the spinel lattice. The magnetic properties are strongly influenced by such variation in the cation distribution as M_s increased (65.7 emu/g) for the sample with the lower inversion degree. In contrast, T_N is increased for the nanocrystals with the higher inversion degree in accordance with the enhancement in the superexchange interactions. The hydrophobic $MnFe_2O_4$ MNPs converted to hydrophilic via CTAB and their NMR relaxivity and hyperthermia effects have been evaluated. Sample S2 with the higher magnetization showed a considerable high r_2 (345.5 mM^{-1} s^{-1}) contrast effect while specific loss power of both samples found concentration dependent. Even in low concentration the nanocrystals produced effective heat response to the external field, while the high magnetization of sample S2 and the lower hydrodynamic size translated to a high heating ability (286 W/g). These results encouraged us to investigate further the potential multifunctional theranostic efficiency of the prepared $MnFe_2O_4$ MNPs.

Acknowledgements

References

[1] M. Colombo, S. Carregal-Romero, M. F. Casula, L. Gutiérrez, M. P. Morales, I. B. Böhm, J. T. Heverhagen, D. Prosperi and W. J. Parak, *Chem. Soc. Rev.,* 2012, **41,** 4306.

[2] E. Amstad, J. Kohlbrecher, E. Müller, T. Schweizer, M. Textor and E. Reimhult, *Nano Lett.,* 2011, **11,** 1664.

[3] S. Laurent, D. Forge, M. Port, A. Roch, C. Robic, L. V. Elst and R. N. Muller, *Chem. Rev.* 2008, **108,** 2064.

[4] J. Jang, H. Nah, J. H. Lee, S. H. Moon, M. G. Kim and J. Cheon, *Angew. Chem. Int. Ed.,* 2009, **48,** 1234.

[5] D. Yoo, J. H. Lee, T. H. Shin and J. Cheon, *Acc. Chem. Res.,* 2011, **44,** 863.

[6] C. G. Hadjipanayis, M. J. Bonder, S. Balakrishnan, X. Wang, H. Mao and G. C. Hadjipanayis, *Small,* 2008, **4,** 1925.

[7] L. Lartigue *et al, J. Am. Chem. Soc.,* 2011, **133,** 10459.

[8] D. Carta, M. F. Casula, P. Floris, A. Falqui, G. Mountjoy, A. Boni, C. Sangregorio and A. Corrias, *Phys. Chem. Chem. Phys.,* 2010, **12,** 5074.

[9] K. E. Sickafus and J. M. Wills, *J. Am. Ceram. Soc.,* 1999, **82,** 3279.

[10] P. J. Zaag, A. Noordermeer, M. T. Johnson and P. F. Bongers, *Phys. Rev. Lett.,* 1992, **68,** 3112.

[11] R. W. Grimes, A. B. Anderson and A. H. Heuer, *J. Am. Chem. Soc.,* 1989, **111,** 1.

[12] T. A. S. Ferreira, J. C. Waerenborgh, M. H. R. M. Mendonça, M. R. Nunes and F. M. Costa, *Solid State Sci.,* 2003, **5,** 383.

[13] D. Carta, M. F. Casula, A. Falqui, D. Loche, G. Mountjoy, C. Sangregorio and A. Corrias, *J. Phys. Chem. C,* 2009, **113,** 8606.

[14] J. P. Chen, C. M. Sorensen, K. J. Klabunde, G. C. Hadjipanayis, E. Devlin and A. Kostikas, *Phys. Rev. B,* 1996, **54,** 9288.

[15] Z. J. Zhang, Z. L. Wang, B. C. Chakoumakos and J. S. Yin, *J. Am. Chem. Soc.,* 1998, **120,** 1800.

[16] Z. Šimša and V. A. M. Brabers, *IEEE Trans. Magn.,* 1975, **11,** 1303.

[17] J. R. Huang and C. Cheng, *J. Appl. Phys.,* 2013, **113,** 033912.

[18] A. Yang, C. N. Chinnasamy, J. M. Greneche, Y. Chen, S. D. Yoon, Z. Chen, K. Hsu, Z. Cai, K. Ziemer, C. Vittoria and V. G. Harris V G*, Nanotechnology,* 2009, **20,** 185704.

[19] V. Georgiadou, C. Kokotidou, B. Le Droumaguet, B. Carbonnier, T. Choli-Papadopoulou and C. Dendrinou-Samara, *Dalton Trans.*, 2014, **43**, 6377.

[20] M. Menelaou, K. Georgoula, K. Simeonidis and C. Dendrinou-Samara, *Dalton Trans.,* 2014, **43**, 3626.

[21] Z. Iatridi, V. Georgiadou, M. Menelaou, C. Dendrinou-Samara and G. Bokias, *Dalton Trans.,* 2014, DOI: 10.1039/c4dt00393d.

[22] B. Xu and X. Wang, *Dalton Trans.,* 2012, **41,** 4719.

[23] A. L. Ankudinov, B. Ravel, J. J Rehr, S. D. Conradson, *Phys. Rev. B,* 1998, **58,** 7565.

[24] S. Mourdikoudis and L. M. Liz-Marzán, *Chem. Mater.,* 2013, **25**, 1465.

[25] V. Šepelák, D. Baabe, D. Mienert, D. Schultze, F. Krumeich, F. J. Litterst and K. D. Becker, *J. Magn. Magn. Mater.,* 2003, **257,** 377.

[26] A. Fairweather, F. F. Roberts and A. J. E. Welch, *Rep. Prog. Phys.,* 1952, **15,** 142.

[27] S. H. Yang*,* D. Heo, E. Lee1, E. Kim, E. K. Lim, Y. H. Lee, S. Haam, J. S. Suh1, Y. M. Huh, J. Yang and S. W. Park, *Nanotechnology,* 2013, **24,** 475103.

[28] R. D. Waldron *Phys Rev.* 1955, **99,** 1727.

[29] C. Kim, M. Min, Y. W. Chang, K. H. Yoo and H. Lee, *J. Nanosci. Nanotechnol.,* 2010, **10,** 233.

[30] G. T. Palomino, S. Bordiga, A. Zecchina, G. L. Marra and C. Lamberti, *J. Phys. Chem. B,* 2000, **104,** 8641.

[31] E. Chalmin, F. Farges and Jr G. E. Brown *Contrib. Mineral. Petrol.,* 2009, **157,** 111.

[32] M. Belli, A. Scafati, A. Bianconi, S. Mobilio, L. Palladino, A. Reale and E. Burattini, *Solid State Commun.,* 1980, **35**, 355.

[33] W. Wolski, E. Wolska, J. Kaczmarek and P. Piszora, *Phys. Stat. Sol. A*, 1995, **152,** K19.

[34] Q. Song, Y. Ding, Z. L. Wang and Z. J. Zhang, *Chem. Mater.,* 2007, **19,** 4633.

[35] R. G. Charles and M. A. Pawlikowski, *J. Phys. Chem.,* 1958, **62,** 440.

[36] K. Ramesh, F. Chen, A. Borgna, C. Srilakshmi and Y. F. Han, *Top. Catal.,* 2008, **49,** 209.

[37] W. S. Seo, H. H. Jo, K. Lee, B. Kim, S. J. Oh and J. T. Park, *Angew. Chem. Int. Ed.,* 2004, **43,** 1115.

[38] M. Bellusci, S. Canepari, G. Ennas, A. Barbera, F. Padella, A. Santini, A. Scano, L. Seralessandri and F. Varsano, *J. Am. Ceram. Soc.,* 2007, **90,** 3977.

[39] N Pinna, G. Garnweitner, M. Antonietti and M. Niederberger, *J. Am. Chem. Soc.,* 2005, **127,** 5608.

[40] H. Li, H. Wu and G. Xiao, *Powder Technol.,* 2010, **198,** 157.

[41] M. Fittipaldi, C. Innocenti, P. Ceci, C. Sangregorio, L. Castelli, L. Sorace and D. Gatteschi, *Phys. Rev. B,* 2011, **83,** 104409.

[42] F. Tournus and E. Bonet, *J. Magn. Magn. Mater.,* 2011, **323,** 1109.

[43] E. L. Duarte, R. Itri, E. Jr. Lima, M. S. Baptista, T. S. Berquó and G. F. Goya, *Nanotechnology* 2006, **17**, 5549.

[44] J. P. Fortin, C. Wilhem, J. Servais, C. Ménager, J. C. Bacri and F. Gazeau, *J. Am. Chem. Soc.* 2007, **129**, 2628.

[45] Z. Beji, A. Hanini, L.S. Smiri, J. Gavard, K. Kacem, F. Villain, J. M. Grenéche, F. Chau and S. Ammar, *Chem. Mater.,* 2010, **22**, 5420.

[46] A. B. Groenou, P. F. Bongers and A. L. Stuyts, *Mater. Sci. Eng.,* 1968, **3,** 317.

[47] C. Pereira, A. M. Pereira, C. Fernandes, M. Rocha, R. Mendes, M. P. Fernández-García, A. Guedes, P. B. Tavares, J.-M. Grenèche, J. P. Araújo and C. Freire*, Chem. Mater.,* 2012, **24,** 1496.

[48] L. Néel, *C. R. Acad. Sci. Paris,* 1950, **230**, 375.

[49] J. M. Hastings and L. M. Corliss, *Phys. Rev.,* 1956, **104,** 328.

[50] F. W. Harrison, W. P. Osmond and R. W. Teale, *Phys. Rev.,* 1957, **106,** 865.

[51] G. A. Sawatzky, F. Van Der Woode, A. H. Morrish, *Phys. Rev.,* 1969, **187,** 747.

[52] A. T. Raghavender and N. H. Hong, *J. Magn. Magn. Mater.,* 2011, **323,** 2145.

[53] C. Kittel, *Introduction to Solids State Physics*, Wiley, Hoboken, 2005.

[54] C. Vázquez-Vázquez, M. A. López-Quintela, M. C. Buján-Núñez and J. Rivas, *J. Nanopart. Res.,* 2011, **13,** 1663.

[55] R. Aquino, J. Depeyrot, M. H. Sousa, F. A. Tourinho, E. Dubois and R. Perzynski, *Phys. Rev. B,* 2005, **72,** 184435.

[56] A. Roch, R. N. Muller and P. Gillis, *J. Chem. Phys.,* 1999, **110,** 5403.

[57] S. H. Koenig and K. E. Keller, *Magn. Reson. Med.,* 1995, **34,** 227.

[58] A. G. Roca, S. Veintemillas-Verdaguer, M. Port, C. Robic, C. J. Serna and Maria P. Morales, *J. Phys. Chem. B*, 2009, **113**, 7033.

[59] S. L. C. Pinho, G. A. Pereira, P. Voisin, J. Kassem, V. Bouchaud, L. Etienne, J. A. Peters, L. Carlos, S. Mornet, C. F. G. C. Geraldes, J. Rocha and M.-H. Delville, ACS Nano, 2010, **4**, 5339.

[60] D. Kim, H. Zeng, T. Ng and C. Brazel, *J. Magn. Magn. Mater.,* 2009, **321**, 3899.

[61] T. Ahmad, Y. Iqbal, H. Bae, I. Rhee, S. Hong, Y. Chang and Jaejun Lee, *J. Korean Phys. Soc.,* 2013, **62**, 1696.

[62] F. Gazeau, M. Lévy and C. Wilhelm, *Nanomedicine,* 2008, **3,** 831.

[63] X. L. Liu, H. M. Fan, J. B. Yi, Y. Yang, E. S. G. Choo, J. M. Xue, D. D. Fan and J. Ding, *J. Mater. Chem.,* 2012, **22,** 8235.

[64] N. D. Thorat, V. M. Khot, A. B. Salunkhe, A. I. Prasad, R. S. Ningthoujam and S. H. Pawar, *J. Phys. D: Appl. Phys.,* 2013, **46,** 105003.

[65] Y. Pineiro-Redondo, M. Bañobre-López, I. Pardinas-Blanco, G. M. A. Goya, M. A. López-Quintela and J. Rivas, *Nanoscale Res. Lett.,* 2011, **6,** 383; K. D. Bakoglidis, K. Simeonidis, D. Sakellari, G. Stefanou and M. Angelakeris, *IEEE Trans. Magn.,* 2012, **48,** 1320.

[66] C. Martinez-Boubeta, K. Simeonidis, A. Makridis, M. Angelakeris, O. Iglesias, P. Guardia, A. Cabot, L. Yedra, S. Estradé, F. Peiró, Z. Saghi, P. A. Midgley, I. Conde-Leborán, D. Serantes and D. Baldomir, *Sci. Rep.,* 2013, **3,** 1652.

[67] A. Doaga, A.M. Cojocariu, W. Amin, F. Heib, P. Bender, R. Hempelmann and O.F. Caltun, *Mater. Chem. Phys.,* 2013, **143**, 305.

[68] D. H. Kim, D. E. Nikles and C. S. Brazel, *Materials,* 2010, **3**, 4051.

[69] D.H. Kim, Y. T. Thai, D. E. Nikles and C. S. Brazel, *IEEE Trans. Magn.,* 2009, **45**, 64.

[70] L. C. Branquinho, M. S. Carriáo, A. S. Costa, N. Zufelato, M. H. Sousa, R. Miotto, R. Ivkov and A. F. Bakuzis, *Sci. Rep.*, 2013, **3**, 2887.

Graphical abstract
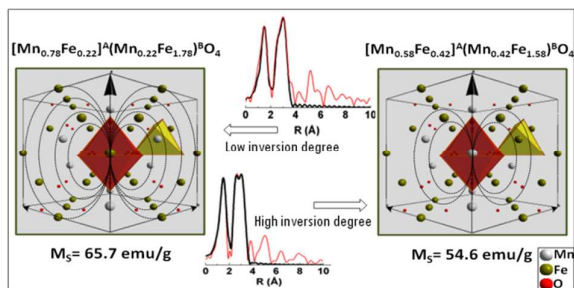
$MnFe_2O_4$ nanoparticles of low inversion degree present optimized magnetization with high (T_2) relaxation (345.5 $s^{-1}mM^{-1}$) and heating efficiency (286 W/g).